

## Full Length Article

## Surface charge recombination matters for single-versus polycrystalline catalysts in the case study of hematite photoanodes

Yawen Dai<sup>a,1</sup>, Guancai Xie<sup>a,1</sup>, Xinrui Jia<sup>a</sup>, Beidou Guo<sup>a</sup>, Jian Ru Gong<sup>a,b,\*</sup><sup>a</sup> Chinese Academy of Sciences (CAS) Center for Excellence in Nanoscience, CAS Key Laboratory for Nanosystem and Hierarchical Fabrication, National Center for Nanoscience and Technology, Beijing 100190, China<sup>b</sup> University of CAS, Beijing 100049, China

## ARTICLE INFO

## Keywords:

Single-polycrystalline catalyst  
Hematite  
Gas phase cation exchange  
Solar water splitting  
Water oxidation  
Photoanode

## ABSTRACT

Charge recombination is a critical problem limiting the efficiency of catalysts for solar water splitting. Constructing both single- and polycrystalline structures have been proposed to tackle this issue, however, comparison of the two is mainly focused on the crystallinity and a comprehensive analysis of the underlying reasons is lacking. Herein, we show that the enhancement in water-oxidation activity of the single crystalline photoanode is dominated by the lower surface charge recombination as compared to the polycrystalline one, taking hematite nanorod arrays prepared by gas phase cation exchange to exclude the influence of shape as the model catalyst. In contrast, the unexpected lower bulk charge separation efficiency of single crystal than that of polycrystal indicates that increasing the crystallinity is actually not the major factor for improving bulk charge transport efficiency. Our study sheds light on the structure–property relationship of monocrystal versus polycrystal in the hematite photoelectrochemical cell, beneficial to design of high-efficient catalysts for solar energy conversion.

## 1. Introduction

Photoelectrochemical (PEC) water splitting is a promising way to solve the energy and environmental crisis [1,2]. Due to the severe recombination of photogenerated charges, however, the efficiency of PEC water splitting systems is still far from satisfying the requirements for the commercialization. It has been suggested that charge recombination can be effectively reduced by nanostructuring [3], defect engineering [4], building hetero- [5] or homojunctions [6], and so on. Among these strategies, constructing single crystalline structures without grain boundaries could offer unique advantages to the PEC activity in terms of the quality of the semiconductor, such as better charge transport property compared to the polycrystalline counterparts which have large numbers of grain boundaries and high charge transport resistance [7,8]. Consequently, photoelectrodes with various single crystalline semiconductors, for example TiO<sub>2</sub> [9,10], WO<sub>3</sub> [11], perovskite [12], and hematite ( $\alpha$ -Fe<sub>2</sub>O<sub>3</sub>) [13], have been widely used in the PEC water splitting with improved PEC performance. However, it was also suggested that polycrystalline photoelectrodes induce a better photocatalytic or PEC activity than the single crystal [14,15], with the

interface defects at crystal boundaries acting as photogenerated electron/hole trappers for yielding long-lived electrons/holes, and thus enhance the charge separation efficiency [16].

Besides crystallinity, the surface area is another important factor regarding the PEC performance [17,18]. Considerable efforts have been spent on preparing nanostructured semiconductors with enlarged surface area to increase the number of active sites for surface reaction [19]. But a large surface area can also limit the PEC activity by increasing surface charge recombination [20]. Compared with the monocrystal, the polycrystal has a larger specific surface area, which would affect the surface properties [17,21]. The influence of the surface area, nevertheless, was never taken into account in previous reports, when investigating the role of crystallinity in PEC systems. With regards to the contradictory statements about the impact of the crystalline structure and the significant role of the surface area in the PEC activity, it is crucial to make an in-depth investigation on the key factor that causes the different properties of the mono- and polycrystal.

In this work, we performed a comprehensive analysis to reveal the key factor influencing the PEC oxygen evolution reaction (OER) efficiency of single- versus polycrystalline hematite nanorod arrays

\* Corresponding author at: Chinese Academy of Sciences (CAS) Center for Excellence in Nanoscience, CAS Key Laboratory for Nanosystem and Hierarchical Fabrication, National Center for Nanoscience and Technology, Beijing 100190, China.

E-mail address: [gongjr@nanoctr.cn](mailto:gongjr@nanoctr.cn) (J.R. Gong).

<sup>1</sup> Contributed equally to this work.

<https://doi.org/10.1016/j.apsusc.2022.155501>

Received 29 September 2022; Received in revised form 24 October 2022; Accepted 26 October 2022

Available online 31 October 2022

0169-4332/© 2022 Elsevier B.V. All rights reserved.

synthesized via gas phase cation exchange to avoid the influence of shape on light absorption and mass transport [22,23]. Hematite is chosen as the model catalyst thanks to its good stability, ruling out the effect of self-corrosion in the PEC process. Single crystalline hematite nanorod arrays (SH) display dramatically higher OER activity as compared to the polycrystalline one (PH), which results from the lower surface charge recombination owing to the smaller surface area and less surface defects of SH [24]. In contrast, the unexpected lower bulk charge separation efficiency of SH than that of PH indicates that increasing the crystallinity is actually not the major factor for improving bulk charge transport efficiency. This work provides helpful guidance for rational design of catalysts for high-efficiency solar energy conversion.

## 2. Experimental

### 2.1. Materials

Zinc acetate ( $\text{Zn}(\text{CH}_3\text{COO})_2 \cdot 2\text{H}_2\text{O}$ ) was provided by Guangdong Engineering Research Center for Fine Chemicals. Ferrous chloride tetrahydrate ( $\text{FeCl}_2 \cdot 4\text{H}_2\text{O}$ ) and ethanolamine were provided by Shanghai Macklin Biochemical Co., Ltd. Zinc nitrate hexahydrate ( $\text{Zn}(\text{NO}_3)_2 \cdot 6\text{H}_2\text{O}$ ) was provided by Tianjin Fuchen Reagent Co., Ltd. Ethylene glycol monomethyl ether was provided by Beijing Kelong Biomedicine Technology Co., Ltd. Hexamethylenetetramine was provided by Shanghai Alfa Aesar Co., Ltd. Fluorine-doped tin oxide conductive glass (FTO) was gained from Huanan Xiangcheng Technology Co., Ltd. The chemicals used in this work were analytically pure and not further purified, and the solutions used in this work were prepared with deionized water.

### 2.2. Preparation of ZnO template

The ZnO nanorod arrays were prepared by a seed-hydrothermal method as reported previously [25]. First, 0.05 M  $\text{Zn}(\text{CH}_3\text{COO})_2$  was dissolved in 20 mL ethylene glycol monomethyl ether and stirred at 60 °C for 30 min. Then, 0.06 mL of ethanolamine was added to the mixture and stirred at 60 °C for another 30 min to get the seed sol. After that, 50  $\mu\text{L}$  of ZnO seed sol was dropped onto an FTO substrate and spin-coated at 1000 rpm for 30 s, which was repeated for 3 times followed by annealing at 350 °C for 30 min. Next, the seed-coated FTO was immersed in a mixed solution of 25 mM  $\text{Zn}(\text{NO}_3)_2$  and 25 mM hexamethylenetetramine, and sealed in an autoclave at 95 °C for 4 h to get the ZnO nanorod array.

### 2.3. Fabrication of hematite photoanodes by gas phase cation exchange

The precursors were placed at the center of a quartz tube, with the  $\text{FeCl}_2$  powder 2.5 cm upstream from the ZnO template. After the quartz tube was outgassed under vacuum, the mixed gas of Ar (5 sccm) and  $\text{O}_2$  (90 sccm) was introduced. The precursors were then heated to 500–600 °C and held for 30 min.

### 2.4. Sample characterization

Scanning electron microscopy (SEM) images and energy-dispersive spectra (EDS) were collected on a Hitachi-SU8220 field emission scanning electron microscope at an accelerating voltage of 10 kV to characterize the micromorphology and elemental composition of the samples. X-ray diffraction (XRD) patterns were recorded on an X'Pert PRO MPD diffractometer with  $\text{Cu K}\alpha$  radiation ( $\lambda = 1.5405 \text{ \AA}$ ). Raman spectra were collected with a Raman Microscope (Renishaw inVia plus) with an excitation wavelength of 785 nm. A FEI Tecnai G2 F20 U-TWIN transmission electron microscope (TEM) operated at 200 kV was used to examine the micromorphology and crystal structure of the samples. X-ray photoelectron spectroscopy (XPS) and valence band spectra measurements were performed on a Thermo Scientific ESCALAB 250 Xi

system using 300 W Al  $\text{K}\alpha$  radiation; the base pressure was  $\sim 3 \times 10^{-9}$  mbar. Binding energies were referenced to the C 1s line at 284.8 eV from adventitious carbon. The ultraviolet–visible (UV–vis) transmittance and reflectance spectra were obtained to calculate the absorbance spectra using a UV–vis spectrophotometer (UV-2600). Photoluminescence (PL) spectra were collected on a photoluminescence spectrometer (Nano-LOG-TCSPC) with an excitation wavelength of 320 nm.

### 2.5. Photoelectrochemical characterization

Photoelectrochemical measurements were performed at room temperature on an electrochemical workstation (Zahner Zennium, Germany) in a three-electrode configuration with the prepared photoanodes as the working electrodes, a saturated Ag/AgCl electrode as the reference electrode, and a Pt foil as the counter electrode. 1M NaOH aqueous solution (pH = 13.6) was used as the electrolyte. A 500 W xenon lamp (CEL-S500, Aulight, Beijing, China) equipped with an AM 1.5G filter was used as the light source, and the distance from the light source to the samples was adjusted to realize an irradiation of 100  $\text{mW cm}^{-2}$  (1 sun). The samples were irradiated from the front side for all the tests. All potentials vs the reversible hydrogen electrode (RHE) were transformed from potentials vs the Ag/AgCl electrode using the following equation:

$$V_{\text{RHE}} = V_{\text{Ag/AgCl}} + 0.059 \times \text{pH} + 0.197 \quad (1)$$

The current density–applied potential ( $J$ – $V$ ) plots of the photoanodes were measured at a scanning rate of 10  $\text{mV s}^{-1}$ . The photoelectrochemical impedance spectroscopy (PEIS) data were collected under 1 sun irradiation using a 5 mV amplitude perturbation between 100 kHz and 0.1 Hz, and the data were fitted using Zview software. Intensity modulated photocurrent spectroscopy (IMPS) measurements were conducted on an electrochemical workstation (Autolab PGSTAT302N) under continuous illumination from a blue LED ( $\lambda = 470 \text{ nm}$ , 80  $\text{mW cm}^{-2}$ ). IMPS spectra were gathered using a 25 % light intensity modulation over a frequency range from 1 kHz to 0.1 Hz.

## 3. Results and discussion

### 3.1. Preparation and characterization of SH and PH photoanodes

With the ZnO nanorod array as the sacrifice template, the hematite nanorod array was in-situ fabricated via a facile gas phase cation exchange methodology [25,26]. The cross-sectional SEM image (Fig. 1a) shows that the ZnO nanorod array has a height of about 1300 nm. After gas phase cation exchange, the obtained hematite nanorod array (Figs. 1(b) and S1) inherits the morphology of the pristine ZnO template, and the semitransparent-white ZnO film (inset of Fig. 1a) turns to orange-red (inset of Fig. 1b) which is the characteristic color of hematite. The EDS spectra in Fig. 1(c and d) depict that the  $\text{Zn}^{2+}$  cations are completely substituted by the  $\text{Fe}^{3+}$  cations. The XRD patterns show that the templates are pure phase of hexagon ZnO (Fig. 1e) and the orange-red film is the hematite (Fig. 1f). On the basis of these data, it is concluded that the ZnO nanorod successfully converts into the hematite nanorod via gas phase cation exchange.

The PH and SH samples were obtained at the cation exchange temperature of 500 °C and 600 °C, respectively. The TEM images (Fig. 2(a and b), S1(e and f)) display a rougher surface of the PH than that of the SH, and many grain boundaries are observed in the PH but not in the SH. The selected area electron diffraction (SAED) pattern of the PH (Fig. 2c) exhibits several rings corresponding to the atomic planes of hematite, demonstrating the polycrystalline nature of the PH. Meanwhile, the SAED pattern of the SH (Fig. 2d) merely presents one set of diffraction pattern and is indexed to the hematite structure with the zone axis of  $[-4-81]$  [27], confirming the single crystalline nature of the SH. Raman spectra (Fig. S2) also confirm the higher crystallinity of the SH than that of the PH. The higher temperature provides higher ion mobility, causing

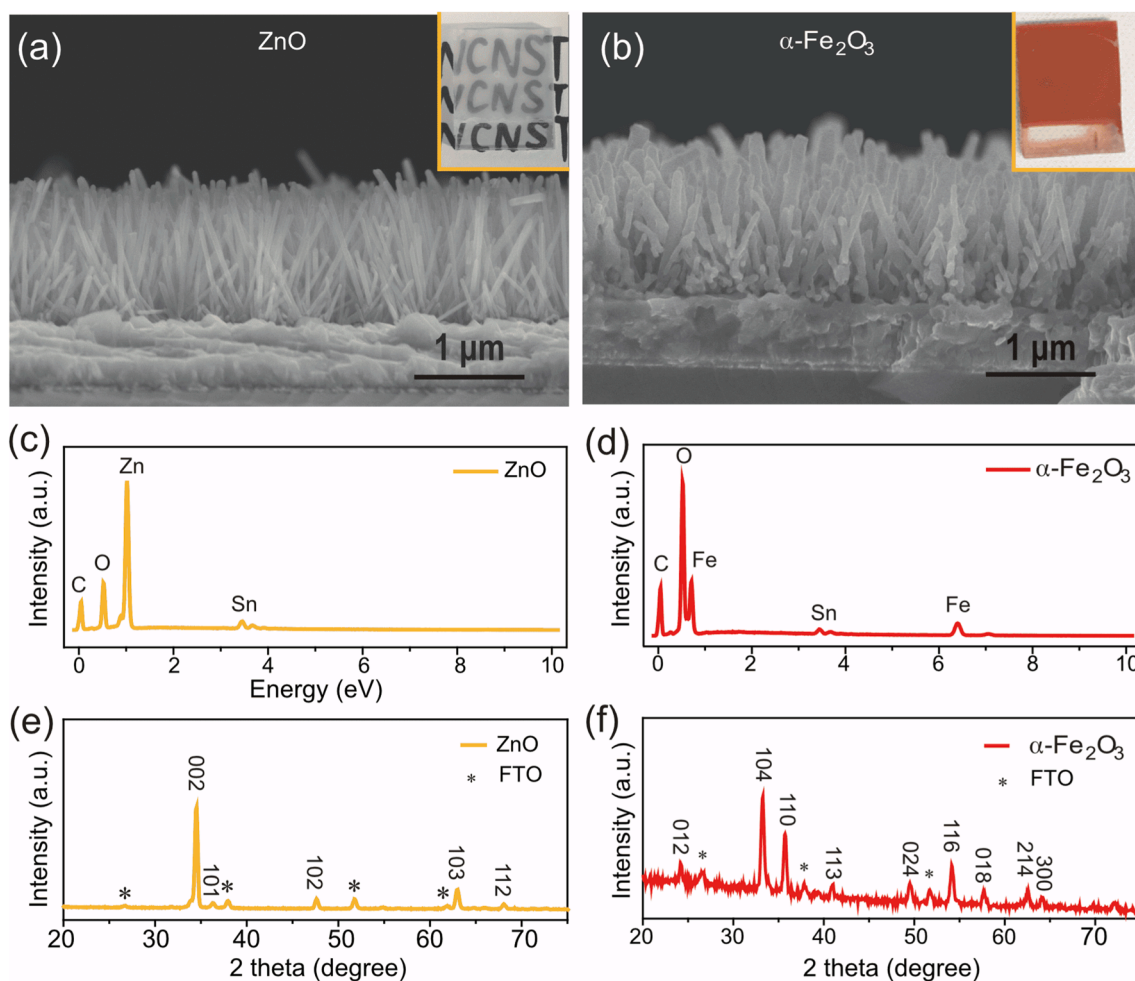


**Fig. 1.** (a, b) Cross-sectional SEM images (Insets are the corresponding digital photographs), (c, d) EDX spectra and (e, f) XRD patterns of the ZnO and  $\alpha$ -Fe<sub>2</sub>O<sub>3</sub> nanorod arrays.

a more effective recrystallization and larger hematite grains and finally resulting in single crystallinity [28]. The high-resolution TEM (HRTEM) image of PH (Fig. 2e) displays one set of lattice stripes with a d-spacing of 0.27 nm that are ascribed to hematite (104) lattice planes. The HRTEM image of SH (Fig. 2f) exhibits two sets of lattice stripes with the same d-spacing of 0.27 nm and an angle of 115°, which are ascribed to hematite (104) and (1-1-4) lattice planes [27]. The lattice stripes with a d-spacing of 0.25 nm in PH are indexed to hematite (-210) lattice planes [27].

### 3.2. OER activity of pH and SH photoanodes

The  $J$ - $V$  curves under irradiation reveal that the PH photoanode has an onset potential of 1.1 V<sub>RHE</sub> and a photocurrent density of  $\sim$ 0.23 mA cm<sup>-2</sup> at 1.23 V<sub>RHE</sub>, whereas the SH photoanode displays an onset potential of  $\sim$ 0.9 V<sub>RHE</sub> and a photocurrent density of  $\sim$ 0.69 mA cm<sup>-2</sup> at 1.23 V<sub>RHE</sub> (Fig. 3). This indicates a significantly higher OER activity of the SH than that of the PH photoanode. The dark currents of both the PH and SH photoanodes were measured to be close to zero over the potential applied in our test, implying that the observed current under irradiation is related to the photogenerated charge carriers.

### 3.3. Mechanism analysis of OER activities

For a photoelectrode, its photocurrent ( $J$ ) for PEC water splitting is determined by the theoretical photocurrent ( $J_{\text{abs}}$ ) depending on light absorption, the bulk separation efficiency ( $\eta_{\text{sep}}$ ), and the surface injection

efficiency ( $\eta_{\text{inj}}$ ), which can be expressed as  $J = J_{\text{abs}} \times \eta_{\text{sep}} \times \eta_{\text{inj}}$  [29]. So, we performed an in-depth analysis on the light absorption,  $\eta_{\text{sep}}$  and  $\eta_{\text{inj}}$  of both PH and SH photoanodes, in attempt to unveil the root cause behind the difference in their OER activities.

Combining the UV-vis spectra, the corresponding Tauc plots of the photoanodes (Fig. S3) and the standard AM 1.5G solar spectrum, the  $J_{\text{abs}}$  values of the PH and SH photoanode were calculated to be 11.99 and 12.05 mA cm<sup>-2</sup>, respectively. The similar  $J_{\text{abs}}$  values for both photoanodes indicates that light absorption is not a determinant reason of their difference in the OER activity. Then, the  $\eta_{\text{sep}}$  and  $\eta_{\text{inj}}$  of the photoanodes were measured from the chopped-light  $J$ - $V$  curves using H<sub>2</sub>O<sub>2</sub> as a sacrificial agent (Fig. S4) [30]. The  $\eta_{\text{sep}}$  of the PH photoanode is slightly higher than that of the SH photoanode (Fig. 4a), which is induced by the lower inter-band radiative recombination rate of the PH as indicated by the PL spectra (Fig. S5) [31]. The trivial difference in the bulk charge separation efficiency between the PH and SH photoanodes is also inconsistent with the disparity in their OER activities. It thus implies that the bulk charge separation efficiency is not the main reason for the difference in their OER activities. As can be seen in Fig. 4(a), the  $\eta_{\text{inj}}$  of the SH photoanode is dramatically higher than that of the PH photoanode, and the changing trend of the  $\eta_{\text{inj}}$ - $V$  curves is similar to that of the irradiated  $J$ - $V$  curves. These findings suggest that the surface injection efficiency is the dominating factor causing the different OER activities between the PH and SH photoanodes.

PEIS were performed to identify the charge transfer behavior both in the bulk hematite and at the hematite/electrolyte interface. The two semicircles in the PEIS-Nyquist plots (Fig. 4b), corresponding to the two

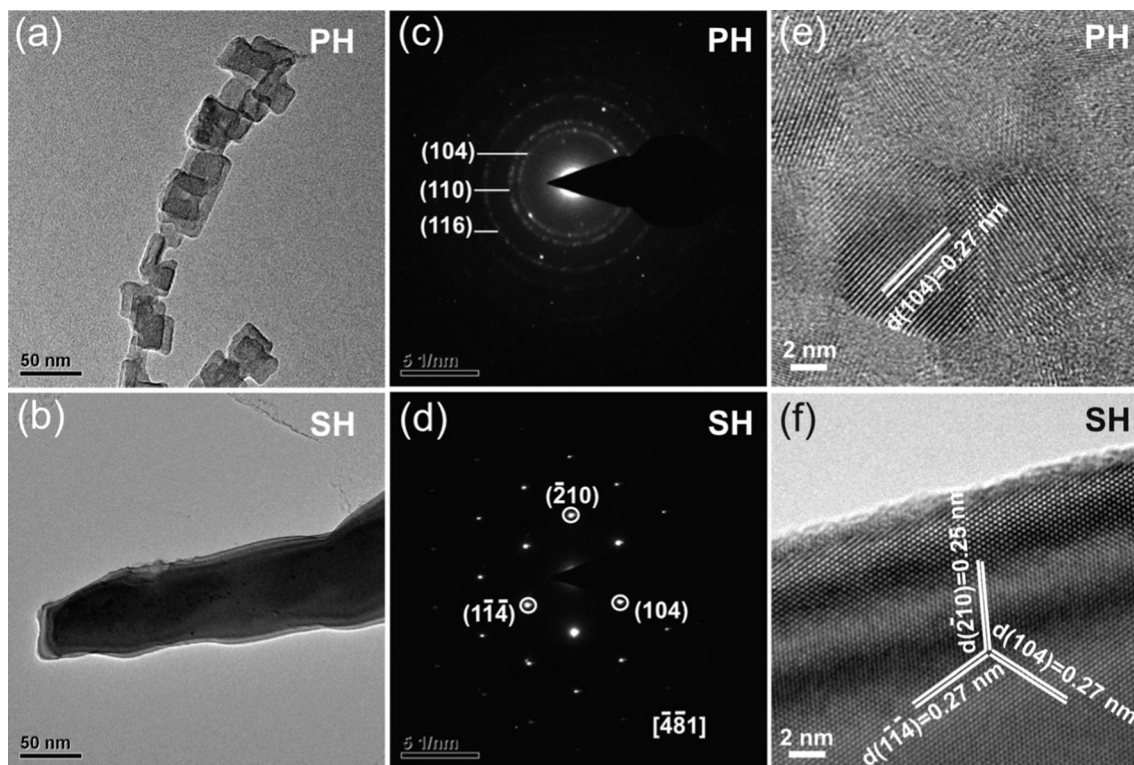


Fig. 2. (a, b) TEM images, (c, d) SAED patterns, and (e, f) HRTEM images of the PH and SH.

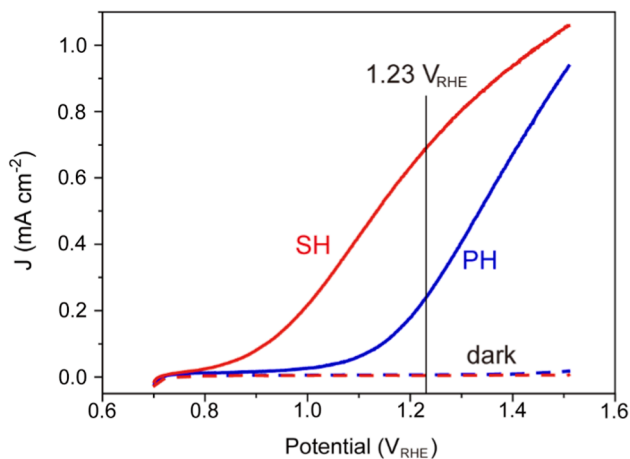


Fig. 3.  $J$ - $V$  curves of the PH and SH photoanodes under irradiation. The red and blue dashed lines represent the corresponding dark current densities. (For interpretation of the references to color in this figure legend, the reader is referred to the web version of this article.)

peaks in their PEIS-Bode plots at high and low frequency ranges (Fig. S6), are ascribed to the charge transport across the bulk hematite and the charge transfer at the hematite/electrolyte interface, respectively [32–34]. PEIS fitting results (Fig. 4c) show a smaller bulk charge transport resistance ( $R_{\text{bulk}}$ ) and a larger surface charge transfer resistance ( $R_{\text{ct}}$ ) of the PH compared to those of the SH photoanode, which is consistent with the higher  $\eta_{\text{sep}}$  and lower  $\eta_{\text{inj}}$  of the PH relative to those of the SH photoanode, as depicted in Fig. 4(a). Namely, the PH has slightly better bulk charge transport and worse surface charge transfer in comparison to the SH photoanode.

The slightly higher  $\eta_{\text{sep}}$  of PH, compared to that of SH, indicates that increasing crystallinity cannot guarantee to improve the bulk charge separation efficiency, which contradicts the generally established result

of previous research [12,35]. One explanation could be the inherently low charge carrier mobility of hematite [36], causing the resistance from grain boundaries exhibits a much less significant effect on the overall charge transport property. Band bending of the depletion layer at the semiconductor/electrolyte interface is the driving force for the bulk charge separation, and hence the bulk charge separation efficiency of the bare hematite is also related to its morphology [37,38]. Due to the similar nanorod array morphology for the SH and PH photoanodes, both surface areas were thus probed to analyze the proportion of the depletion layer to the bulk. For the same material, the surface area of the electrode is in positive proportion to the electrochemical active surface area (ECSA) [39–41]. ECSA of the hematite photoanodes was determined by electrochemical double-layer capacitances measurements (Figs. 4(d) and S7), reflecting a larger ECSA of the PH ( $106 \mu\text{F cm}^{-2}$ ) than that of the SH ( $51 \mu\text{F cm}^{-2}$ ) [42]. In comparison with the SH, the PH photoanode has a larger interface area between the semiconductor and the electrolyte because of more grain boundaries on its rough surface, generating a higher portion of the depletion region to the entire bulk region by provide higher driving force for charges [43], thus contributing to the slightly higher  $\eta_{\text{sep}}$  of the PH than that of the SH photoanode.

Next, we investigated the reason behind the great difference of  $\eta_{\text{inj}}$  between the PH and SH photoanodes. Oxygen vacancy and surface area are reported to be two factors that could influence  $\eta_{\text{inj}}$  for the bare hematite [20,44]. The oxygen vacancies were first analyzed by XPS. As illustrated in Fig. 5(a and b), the peak at low binding energy (ca. 530 eV) can be attributed to oxygen in the hematite lattice ( $\text{O}_L$ ), while the peak at high binding energy (ca. 531.7 eV) is associated with oxygen vacancies ( $\text{O}_V$ ) [44,45]. The percentages of the  $\text{O}_V$  in the PH and SH are approximate, with the value of 43.6 % and 44.3 %, respectively. Little peak shift in the Raman spectra (Fig. S2) suggests the amount of the  $\text{O}_V$  and  $\text{O}_L$  in the SH is very close to those in the PH, which is consistent with the XPS data [44,46]. This result implies that the  $\text{O}_V$  in the PH and SH will have similar impact on their OER activity and hence the possible role of the oxygen vacancy concentration can be eliminated, which

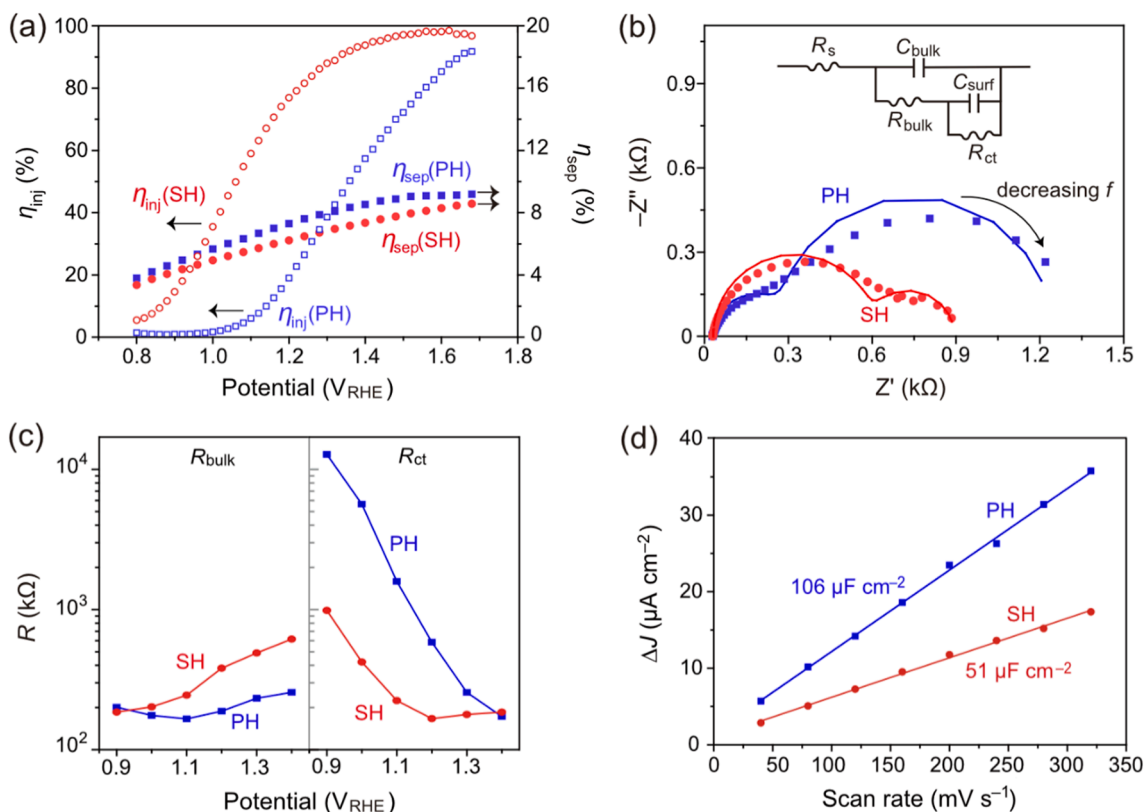


**Fig. 4.** (a) Charge separation and injection efficiencies, (b) measured (dots) and fitted (lines) PEIS-Nyquist plots at 1.2  $V_{RHE}$  (inset shows the equivalent circuit for PEIS fitting), (c) PEIS fitting results of the  $R_{bulk}$  and  $R_{ct}$  values, (d) differences in current as functions of scan rate for the PH and SH photoanodes.

means that the surface area becomes dominant here. The larger surface area of the PH photoanode can benefit charge injection by providing more sites for surface catalytic reaction, which is confirmed by the higher dark currents and faster OER kinetics observed for the PH, as compared to the SH photoanode (Fig. S8). However, the abundant grain boundaries on the PH surface could induce high surface trap density, which leads to non-radiative recombination on the surface [47,48]. As a result, the large surface area might also induce severe surface recombination that decreases the lifetime of surface holes, which is detrimental for the surface hole injection efficiency considering the OER kinetics with a time scale of hundreds of milliseconds to seconds [49,50]. The hole lifetime was then calculated from the spike decay in anodic photocurrent transients by a logarithmic plot of the parameter  $D$ , using the following Equation:

$$D = \frac{J_t - J_{st}}{J_{in} - J_{st}} \quad (2)$$

where  $J_t$  is the photocurrent density at time  $t$ ,  $J_{st}$  is the steady-state photocurrent density, and  $J_{in}$  is the initial spike of the photocurrent density upon light on (inset of Fig. 5c) [51,52]. To get a qualitative comparison, the hole lifetime can be defined as the time at which  $\ln D = -1$  [51,52]. The  $\ln D$  decay plots (Fig. 5c) indicate a hole lifetime of 0.06 s for the PH and 0.12 s for the SH photoanode, which is in tune with the result that the SH has a higher hole injection efficiency than the PH photoanode.

In the end, IMPS was conducted to further evaluate the surface charge recombination due to the non-radiative electron-hole recombination at surface states. As shown in Fig. 5(d), each IMPS spectrum is composed of two semicircles. The low frequency response of the upper semicircle can be ascribed to the charge transfer and recombination at the interface of the electrolyte and the photoanode [53], and the low frequency intercept (LFI) corresponds to the hole current successfully transferred to the electrolyte [54,55]. The high frequency response of

the lower semicircle is called RC attenuation semicircle, which represents attenuation by the total series resistance of the PEC cell and the capacitances of the sample, and the high frequency intercept (HFI) signifies the photogenerated hole flux toward the surface. The charge transfer and recombination behavior can be revealed by analyzing the upper semicircle. The photogenerated hole current of the PH is close to that of the SH photoanode, while the hole current transfer into the electrolyte of the PH photoanode is lower than that of the SH photoanode as manifested in Fig. 5(d). These results imply that the PH has a severe charge recombination than the SH photoanode, which agrees with the bulk charge separation and injection efficiency [56]. The electron lifetime ( $\tau_d$ ) can be estimated from the frequency at the minimal value in the IMPS [57,58]:  $\tau_d = 1/(2\pi f_{min})$ . The electron lifetime of SH (2.7–5.0 ms) is longer than that of the PH photoanode (1–1.5 ms) over the entire applied potentials (Fig. S9). As mentioned above, the larger surface area of the PH would bring more serious surface charge recombination than the SH photoanode, resulting in the shorter electron lifetime, which is consistent with the shorter hole lifetime of the PH than that of the SH photoanode (Fig. 5c). According to the above analysis, we conclude that the drastic surface charge recombination induced by the large surface area is more dominant than the positive effect of providing more active sites, thus translating into the lower surface injection efficiency of the PH relative to that of the SH photoanode.

Based on the above analyses, an explanation for the different PEC OER activity between the SH and PH photoanodes is proposed as follows. Due to the similar light absorption, the SH and PH photoanodes generate nearly the same amount of photocharges upon light irradiation. Compared to the SH, the existence of grain boundaries in the PH photoanode results in the rougher electrode surface and hence the larger surface area. The larger surface area in the PH photoanode increases the portion of the depletion region to the entire bulk region, thus leading to the better charge separation efficiency than the SH with the high crystallinity as schemed in Scheme 1(a). However, the large surface area in

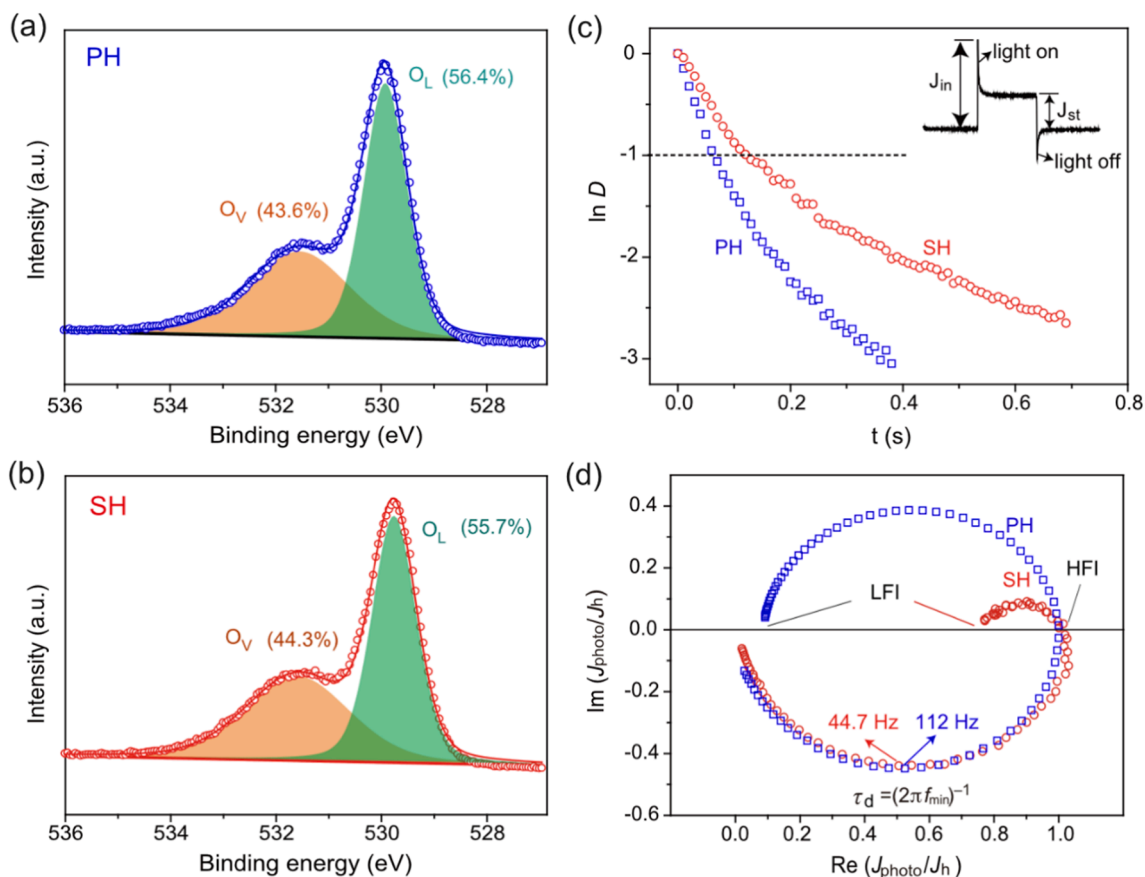
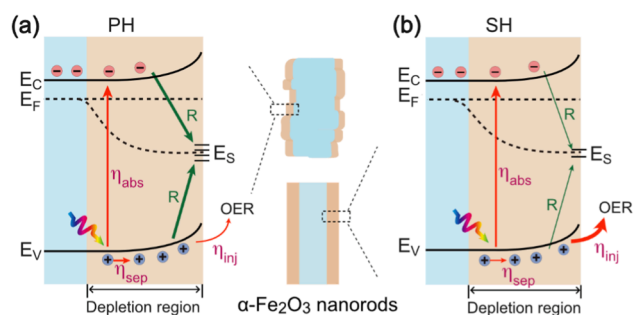


Fig. 5. (a, b) XPS O 1s spectra (the data in brackets are the percentages of  $O_V$  and  $O_L$ ), (c) anodic transient dynamics at 1.0  $V_{RHE}$ , and (d) normalized IMPS spectra at 1.0  $V_{RHE}$  for the PH and SH photoanodes. For the fitting of XPS spectra, the background was removed using a Shirley-type background and the spectra were fitted using two Gaussian-Lorentzian peaks.



**Scheme 1.** Schematics of charge behaviors in (a) PH and (b) SH photoanodes.  $E_C$ ,  $E_V$ ,  $E_F$ , and  $E_S$  represent for the conduction band minimum, the valence band maximum, and the Fermi level of hematite and the surface state levels on the hematite surface, respectively. Red arrows refer to the beneficial contributions including charge generation from photoexcitation ( $\eta_{abs}$ ), bulk charge separation ( $\eta_{sep}$ ), and hole transfer to the electrolyte ( $\eta_{inj}$ ). Green arrows refer to the deleterious contribution, that is, surface charge recombination (R). The arrow line thickness indicates the relative rates of charge transfer and recombination, and the thicker arrow lines represent the faster rates than the thinner ones.

the PH photoanode also brings on severe surface recombination of photocharges because surface states at grain boundaries would act as charge recombination centers. As a consequence, majority of the photoholes on the PH photoanode surface would recombine with the photoelectrons at surface states other than inject to the electrolyte for the OER. By contrast, the SH photoanode show the less surface charge recombination and the better charge injection efficiency thanks to the small surface area and single crystalline property, and hence the higher

PEC OER activity than the PH (Scheme 1b).

#### 4. Conclusions

In summary, the influences of crystallinity on the PEC OER activity were systematically studied by taking the  $\alpha\text{-Fe}_2\text{O}_3$  nanorod array with tunable crystallinity as a model photoelectrode. Thanks to the lower surface charge recombination out of the small surface area and less surface defects, the single crystalline hematite photoanode possesses a significant better surface injection efficiency and thus a higher OER activity than the polycrystalline. This study provides a comprehensive investigation on the understanding of the PEC performance difference between single crystalline and polycrystalline hematite nanorods, and provide useful guidelines for the development of highly efficient PEC devices.

#### CRediT authorship contribution statement

**Yawen Dai:** Investigation, Methodology, Data curation, Formal analysis, Writing – original draft. **Guancai Xie:** Investigation, Validation, Formal analysis, Writing - review & editing. **Xinrui Jia:** Investigation. **Beidou Guo:** Investigation. **Jian Ru Gong:** Resources, Funding acquisition, Supervision, Conceptualization, Investigation, Project administration, Writing - review & editing.

#### Declaration of Competing Interest

The authors declare that they have no known competing financial interests or personal relationships that could have appeared to influence the work reported in this paper.

## Data availability

Data will be made available on request.

## Acknowledgments

This work was supported by the Strategic Priority Research Program of CAS (XDB36000000) and National Natural Science Foundation of China (22102037, 22179028, 22002028).

## Appendix A. Supplementary material

Supplementary data to this article can be found online at <https://doi.org/10.1016/j.apsusc.2022.155501>.

## References

- [1] M. Gratzel, *Nature* 414 (2001) 338–344.
- [2] Y.-Y. Wang, Y.-X. Chen, T. Barakat, Y.-J. Zeng, J. Liu, S. Siffert, B.-L. Su, *J. Energy Chem.* 66 (2022) 529–559.
- [3] A. Kay, I. Cesar, M. Grätzel, *J. Am. Chem. Soc.* 128 (2006) 15714–15721.
- [4] M. Sun, R.-T. Gao, J. He, X. Liu, T. Nakajima, X. Zhang, L. Wang, *Angew. Chem. Int. Ed.* 60 (2021) 17601–17607.
- [5] S.-S. Yi, Z.-Y. Wang, H.-M. Li, Z. Zafar, Z.-T. Zhang, L.-Y. Zhang, D.-L. Chen, Z.-Y. Liu, X.-Z. Yue, *Appl. Catal. B: Environ.* 283 (2021) 119649.
- [6] Y. Wu, X. Liu, H. Zhang, J. Li, M. Zhou, L. Li, Y. Wang, *Angew. Chem.* 133 (2021) 3529–3534.
- [7] T. Wang, J. Gong, *Angew. Chem. Int. Ed.* 54 (2015) 10718–10732.
- [8] X. Sheng, T. Xu, X. Feng, *Adv. Mater.* 31 (2019) e1805132.
- [9] T. Butburee, Y. Bai, H. Wang, H. Chen, Z. Wang, G. Liu, J. Zou, P. Khemthong, G.Q. M. Lu, L. Wang, *Adv. Mater.* 30 (2018) e1705666.
- [10] W. Jiao, Y. Xie, R. Chen, C. Zhen, G. Liu, X. Ma, H.M. Cheng, *Chem. Commun.* 49 (2013) 11770–11772.
- [11] Y. Bu, J. Ren, H. Zhang, D. Yang, Z. Chen, J.P. Ao, *J. Mater. Chem. A* 6 (2018) 8604–8611.
- [12] X.-D. Wang, Y.-H. Huang, J.-F. Liao, Z.-F. Wei, W.-G. Li, Y.-F. Xu, H.-Y. Chen, D.-B. Kuang, *Nat. Commun.* 12 (2021) 1–9.
- [13] D. Wang, Y. Zhang, C. Peng, J. Wang, Q. Huang, S. Su, L. Wang, W. Huang, C. Fan, *Adv. Sci.* 2 (2015) 1500005.
- [14] Y. Li, X.Y. Yang, J. Rooke, G. Van Tendeloo, B.L. Su, *J. Colloid Interface Sci.* 348 (2010) 303–312.
- [15] Z. Zhang, I. Karimata, H. Nagashima, S. Muto, K. Ohara, K. Sugimoto, T. Tachikawa, *Nat. Commun.* 10 (2019) 4832.
- [16] J. Zhuang, S. Weng, W. Dai, P. Liu, Q. Liu, *J. Phys. Chem. C* 116 (2012) 25354–25361.
- [17] C.W. Wang, S. Yang, W.Q. Fang, P. Liu, H. Zhao, H.G. Yang, *Nano Lett.* 16 (2016) 427–433.
- [18] L. Jin, F. Cheng, H. Li, K. Xie, *Angew. Chem. Int. Ed.* 59 (2020) 8891–8895.
- [19] Z.F. Huang, L. Pan, J.J. Zou, X. Zhang, L. Wang, *Nanoscale* 6 (2014) 14044–14063.
- [20] F.E. Osterloh, *Chem. Soc. Rev.* 42 (2013) 2294–2320.
- [21] J.Y. Kim, G. Magesh, D.H. Youn, J.W. Jang, J. Kubota, K. Domen, J.S. Lee, *Sci. Rep.* 3 (2013) 2681.
- [22] X. Sun, Q. Li, J. Jiang, Y. Mao, *Nanoscale* 6 (2014) 8769–8780.
- [23] Z. Liu, K. Wang, L. Xiao, X. Chen, X. Ren, J. Lu, L. Zhuang, *RSC. Adv.* 4 (2014) 37701–37704.
- [24] W. Yu, F. Li, L. Yu, M.R. Niazi, Y. Zou, D. Corzo, A. Basu, C. Ma, S. Dey, M.L. Tietze, U. Buttner, X. Wang, Z. Wang, M.N. Hedhili, C. Guo, T. Wu, A. Amassian, *Nat. Commun.* 9 (2018) 5354.
- [25] H. Zhang, T. Ling, X.W. Du, *Chem. Mater.* 27 (2014) 352–357.
- [26] J.B. Rivest, P.K. Jain, *Chem. Soc. Rev.* 42 (2013) 89–96.
- [27] S. Sun, K.O. Konhauser, A. Kappler, Y.-L. Li, *GSA Bull.* 127 (2015) 850–861.
- [28] T. Supasai, S. Dangtip, P. Learngarunsi, N. Boonyopakorn, A. Wisitsoraat, S. K. Hodak, *Appl. Surf. Sci.* 256 (2010) 4462–4467.
- [29] Y. Hu, Y. Wu, J. Feng, H. Huang, C. Zhang, Q. Qian, T. Fang, J. Xu, P. Wang, Z. Li, Z. Zou, *J. Mater. Chem. A* 6 (2018) 2568–2576.
- [30] H. Dotan, K. Sivula, M. Grätzel, A. Rothschild, S.C. Warren, *Energy Environ. Sci.* 4 (2011) 958–964.
- [31] X. Chang, T. Wang, P. Zhang, J. Zhang, A. Li, J. Gong, *J. Am. Chem. Soc.* 137 (2015) 8356–8359.
- [32] K. Zhang, T. Dong, G. Xie, L. Guan, B. Guo, Q. Xiang, Y. Dai, L. Tian, A. Batool, S. U. Jan, R. Boddula, A.A. Thebo, J.R. Gong, A.C.S. Appl. Mater. Interfaces 9 (2017) 42723–42733.
- [33] F. Malara, A. Minguzzi, M. Marelli, S. Morandi, R. Psaro, V. Dal Santo, A. Naldoni, *ACS Catal.* 5 (2015) 5292–5300.
- [34] Y. Dai, J. Yu, C. Cheng, P. Tan, M. Ni, *J. Mater. Chem. A* 8 (2020) 6984–7002.
- [35] X. Xu, W. Wang, Y. Zhang, Y. Chen, H. Huang, T. Fang, Y. Li, Z. Li, Z. Zou, *Sci. Bull.* 67 (2022) 1458–1466.
- [36] C. Li, Z. Luo, T. Wang, *J. Gong. Adv. Mater.* 30 (2018) e1707502.
- [37] A. Liao, H. He, Y. Zhou, Z. Zou, *J. Semicond.* 41 (2020), 091709.
- [38] C. Li, Z. Luo, T. Wang, *J. Gong. Adv. Mater.* 30 (2018) 1707502.
- [39] H. She, P. Yue, X. Ma, J. Huang, L. Wang, Q. Wang, *Appl. Catal. B: Environ.* 263 (2020) 118280.
- [40] L. Mao, Y. Huang, Y. Fu, C. Dong, S. Shen, *Sci. Bull.* 64 (2019) 1262–1271.
- [41] C. Wei, S. Sun, D. Mandler, X. Wang, S.Z. Qiao, Z.J. Xu, *Chem. Soc. Rev.* 48 (2019) 2518–2534.
- [42] F. Ning, M. Shao, S. Xu, Y. Fu, R. Zhang, M. Wei, D.G. Evans, X. Duan, *Energy Environ. Sci.* 9 (2016) 2633–2643.
- [43] C. Li, A. Li, Z. Luo, J. Zhang, X. Chang, Z. Huang, T. Wang, *J. Gong. Adv. Chem. Int. Ed.* 56 (2017) 4150–4155.
- [44] Z. Wang, X. Mao, P. Chen, M. Xiao, S.A. Monny, S. Wang, M. Konarova, A. Du, L. Wang, *Angew. Chem.* 58 (2019) 1030–1034.
- [45] R. Gao, L. Pan, Z. Li, C. Shi, Y. Yao, X. Zhang, J.-J. Zou, *Adv. Funct. Mater.* 30 (2020) 1910539.
- [46] X. Lu, Y. Zeng, M. Yu, T. Zhai, C. Liang, S. Xie, M.S. Balogun, Y. Tong, *Adv. Mater.* 26 (2014) 3148–3155.
- [47] M. Fathabadi, M. Qorbani, A. Sabbah, S. Quadir, C.-Y. Huang, K.-H. Chen, L.-C. Chen, N. Naseri, *J. Mater. Chem. A* 10 (2022) 16655–16665.
- [48] Y.-F. Xu, X.-D. Wang, H.-Y. Chen, D.-B. Kuang, C.-Y. Su, *Adv. Funct. Mater.* 26 (2016) 4414–4421.
- [49] F. Le Formal, S.R. Pendlebury, M. Cornuz, S.D. Tilley, M. Gratzel, J.R. Durrant, *J. Am. Chem. Soc.* 136 (2014) 2564–2574.
- [50] S.R. Pendlebury, A.J. Cowan, M. Barroso, K. Sivula, J. Ye, M. Grätzel, D.R. Klug, *J. Tang, J.R. Durrant, Energy Environ. Sci.* 5 (2012) 6304–6312.
- [51] Z. Xu, H. Wang, Y. Wen, W. Li, C. Sun, Y. He, Z. Shi, L. Pei, Y. Chen, S. Yan, Z. Zou, A.C.S. Appl. Mater. Interfaces 10 (2018) 3624–3633.
- [52] Z. Xu, Z. Fan, Z. Shi, M. Li, J. Feng, L. Pei, C. Zhou, J. Zhou, L. Yang, W. Li, G. Xu, S. Yao, Z. Zou, *ChemSusChem* 11 (2018) 237–244.
- [53] L.M. Gurudayal, L.H. Peter, F.F.A. Wong, *ACS Appl. Mater. Interfaces* 9 (2017) 41265–41272.
- [54] R. Yalavarthi, A. Naldoni, R. Zboril, S. Kment, *Catal. Today* 361 (2021) 117–123.
- [55] Y. Dai, P. Cheng, G. Xie, C. Li, M.Z. Akram, B. Guo, R. Boddula, X. Shi, J. Gong, J. R. Gong, *J. Phys. Chem. C* 123 (2019) 28753–28762.
- [56] J.E. Thorne, J.W. Jang, E.Y. Liu, D. Wang, *Chem. Sci.* 7 (2016) 3347–3354.
- [57] J. Kruger, R. Plass, M. Gratzel, P.J. Cameron, L.M. Peter, *J. Phys. Chem. B* 107 (2003) 7536–7539.
- [58] G. Liu, S. Ye, P. Yan, F. Xiong, P. Fu, Z. Wang, Z. Chen, J. Shi, C. Li, *Energy Environ. Sci.* 9 (2016) 1327–1334.